DESIGN AND ANALYSIS OF UAV-AIDED RIS NOMA COMMUNICATION SYSTEM

M.Tech Thesis

by

EGU DHEERAJ KUMAR

DEPARTMENT OF ELECTRICAL ENGINEERING
INDIAN INSTITUTE OF TECHNOLOGY INDORE
MAY 2024

DESIGN AND ANALYSIS OF UAV-AIDED RIS NOMA COMMUNICATION SYSTEM

A THESIS

Submitted in partial fulfillment of the

requirements for the award of the degree

of

MASTER OF TECHNOLOGY

by

EGU DHEERAJ KUMAR

DEPARTMENT OF ELECTRICAL ENGINEERING
INDIAN INSTITUTE OF TECHNOLOGY INDORE
MAY 2024

INDIAN INSTITUTE OF TECHNOLOGY INDORE

CANDIDATE'S DECLARATION

I hereby certify that the work which is being presented in the thesis entitled **"DESIGN AND ANALYSIS OF UAV-AIDED RIS NOMA COMMUNICATION SYSTEM"** in the partial fulfillment of the requirements for the award of the degree of **MASTER OF TECHNOLOGY** and submitted in the **DEPARTMENT OF ELECTRICAL ENGINEERING, Indian Institute of Technology Indore**, is an authentic record of my own work carried out during the time period from July 2022 to May 2024 under the supervision of Prof. Prabhat Kumar Upadhyay, Professor, Department of Electrical Engineering, Indian Institute of Technology Indore, India.

The matter presented in this thesis has not been submitted by me for the award of any other degree of this or any other institute.

E. Dheeraj. 22/5/2024

Signature of the student with date

(EGU DHEERAJ KUMAR)

This is to certify that the above statement made by the candidate is correct to the best of my/our knowledge.

22/5/2024

Signature of Thesis Supervisor with date

(Prof. PRABHAT KUMAR UPADHYAY)

EGU DHEERAJ KUMAR has successfully given his M.Tech. Oral Examination held on ... May 7, 2024.

Signature of Thesis Supervisor with date

(Prof. PRABHAT KUMAR UPADHYAY)

ACKNOWLEDGEMENTS

I take this opportunity to acknowledge my heartfelt gratitude to all those who have directly or indirectly helped me throughout my MTech. First and foremost, I thank God Almighty for giving me the strength, knowledge, and enlightenment to undertake this research work. Then, I would like to express my deep sense of respect and gratitude to my supervisor and mentor, Prof. Prabhat Kumar Upadhyay, for his invaluable guidance, sustained inspiration, and kind support towards my thesis work. He has given me all the freedom to pursue my research, and provided helpful career advice and suggestions, extending beyond academic boundaries, whenever needed. He has always been my source of inspiration during my stay at IIT Indore and will be, all my life.

Next, I would like to sincerely thank my PSPC member committee for their interesting discussions and suggestions towards my research. I am thankful to all the faculty members and the staff at IIT Indore for their cooperation throughout my thesis work.

My appreciation also goes to all the members of the Wireless Communications (WiCom) Research Group for creating a friendly and conducive environment. It was my privilege to share the lab with Cheepurupalli Shivaji and Kajal Yadav.

I am extremely thankful to all my batchmates and unitmates for making a wonderful company and sharing all the casual and valued moments which helped me during the hardship of this work and my life at IIT Indore.

I would like to thank the Ministry of Human Resource Development (MHRD), Government of India and IIT Indore for providing financial assistance. I will also thank the finance, administration, academic, and R&D sections for all the necessary support.

Above all, the most valued gratitude is expressed for my family for their endless support and faith in me, without which I would have not been able to achieve the greatest milestone of my life.

Lastly, I want to thank everyone who were part of this journey and has, in one way or another, helped me to successfully complete this research work.

Egu Dheeraj Kumar

ABSTRACT

Modern wireless networks must be put in place to accommodate the fast rising data traffic produced by the growth of mobile applications and their integration into many aspects of everyday life. The most important characteristics to consider while building future communication systems are access to high-speed internet, huge capacity, low signal delay, prolonged battery life, wide coverage, and so on.

Open wireless environments are known to be uncontrollable and in this era of increasing demands, programmable radio environments using reflective intelligent surface (RIS) are being explored. To save spectral resources in beyond 5G scenarios, non-orthogonal multiple access (NOMA) is a technique that is predicted to be applied. Given the nature of wireless propagation, it is expected that the security of data transmitted has a possibility of being compromised by the presence of eavesdropping illegitimate devices. So, it is imperative to explore methods of securing data at the physical layer level.

The purpose of this thesis is to investigate data security in a NOMA network that includes a RIS and an unmanned aerial vehicle (UAV) to aid the weaker user. In addition, a jammer whose signal is detectable to authorized users is used to impair the eavesdropper's efforts of intercepting the signal. System performance is assessed using mathematical equations for the secrecy outage probability (SOP). Further, asymptotic SOP analysis is done to identify how crucial parameters affect overall system performance. The influence of various signal power intensities, power distribution values, and number of reflecting RIS elements on system performance is explored. Finally, a deep neural network (DNN) framework is developed for SOP prediction and quick execution in such dynamic situations.

CONTENTS

LIST OF FIGURES

List of Symbols

- Basic arithmetic and calculus notations have standard definitions.

Elementary & Special Functions

Notation	Definition
$\Gamma(\cdot)$	Gamma function
$\Upsilon(\cdot,\cdot)$	lower incomplete Gamma function
$I_v(.)$	modified v-order Bessel function of the first kind
$\log_i(\cdot)$	logarithm to base i

Probability & Statistics

Let X be a random variable, and $\mathcal{A}$ be an arbitrary event.

Notation	Definition
$E\{\cdot\}$	expectation
$f_X(\cdot)$	probability density function (PDF) of X
$F_X(\cdot)$	cumulative distribution function (CDF) of X
$\Pr\{\mathcal{A}\}$	probability of $\mathcal{A}$
$X \sim \mathcal{CN}(\mu, \sigma^2)$	X is complex Gaussian distributed with mean μ and variance σ^2

Miscellaneous

Notation	Definition
$\lvert\cdot\rvert$	absolute value
$[x]^+$	$\max\{x, 0\}$
$n!$	factorial of n

Acronyms

5G	Fifth-Generation
6G	Sixth-Generation
AWGN	Additive White Gaussian Noise
BS	Base Station
CDF	Cumulative Distribution Function
CSI	Channel State Information
DL	Deep Learning
DLS	Damped Least Squares
DNN	Deep Neural Network
DoS	Denial of Serivce
DSSS	Direct-Sequence Spread Spectrum
eLU	Exponential Linear Unit
FHSS	Frequency Hopping Spread Spectrum
HAP	High Altitude Platforms
IoT	Internet of Things
LAP	Low Altitude Platforms
LoS	Line-of-Sight
ML	Machine Learning
NOMA	Non-Orthogonal Multiple Access
OMA	Orthogonal Multiple Access
PDF	Probability Density Function
PLS	Physical Layer Security
RF	Radio-Frequency
RIS	Reconfigurable Intelligent Surfaces
RMSE	Root Mean Square Error
SC	Superposition Coding
SIC	Successive Interference Cancellation
SINR	Signal-to-Interference-Plus-Noise Ratio
SNR	Signal-to-Noise Ratio
SOP	Secrecy Outage Probability
UAV	Unmanned Aerial Vehicles

CHAPTER 1

INTRODUCTION AND BACKGROUND

1.1 Introduction

The rapid development of fifth-generation (5G) wireless technology has increased customer appetite for mobile internet, wireless rapid payment and virtual reality applications. By 2030, 500 billion devices are expected to be linked, with each mobile user consuming 257 GB of data monthly. [1]. In addition, estimates suggest that around 15.14 billion Internet of Things (IoT) devices will be interconnected globally. This figure is expected to nearly double by 2030 to 29.42 billion [2]. In these unforeseen situations, the next phase of wireless communication systems must make efficient use of both energy and spectrum.

Traditionally, wireless system development has been predicated on the idea that radio surroundings are rigid and uncontrolled, with the primary goal of minimizing their negative consequences. To take full advantage of the potential of future wireless networks, it is vital to investigate the possibilities of developing controlled and programmable radio environments, which will serve as a new dimension for system efficiency. Also, due to increasing radio frequency in the upcoming generations, the effects of diffraction and scattering decrease, making electromagnetic waves more susceptible to being blocked by obstructions like as buildings in cities. As a result, standard cellular approaches make it difficult to achieve universal coverage of wireless services in 5G and beyond.

1.1.1 Reconfigurable Intelligent Surfaces

Reconfigurable intelligent surface (RIS) is a novel technology that is expected to be employed in the sixth generation (6G) scenario. [3]. In recent years, RIS has been proposed as a way to improve wireless signal transmission efficiency. RIS are composed of planar synthetic metasurfaces with several programmable reflection amplitude/phase changes controlled by a sophisticated controller. They may change the phase and amplitude of incident signals. This capability enhances intended signals while reducing interference, offering disruptive possibilities for wireless network architecture. Furthermore, their simple application in the geographical locations of contemporary wireless networks is extremely beneficial to increasing the effectiveness of bandwidth and energy resources. However, the majority of the available literature has focused on the RIS being fixed in certain places, which limits its capacity to modify the radio environment more efficiently. Reconfigurable electromagnetic materials

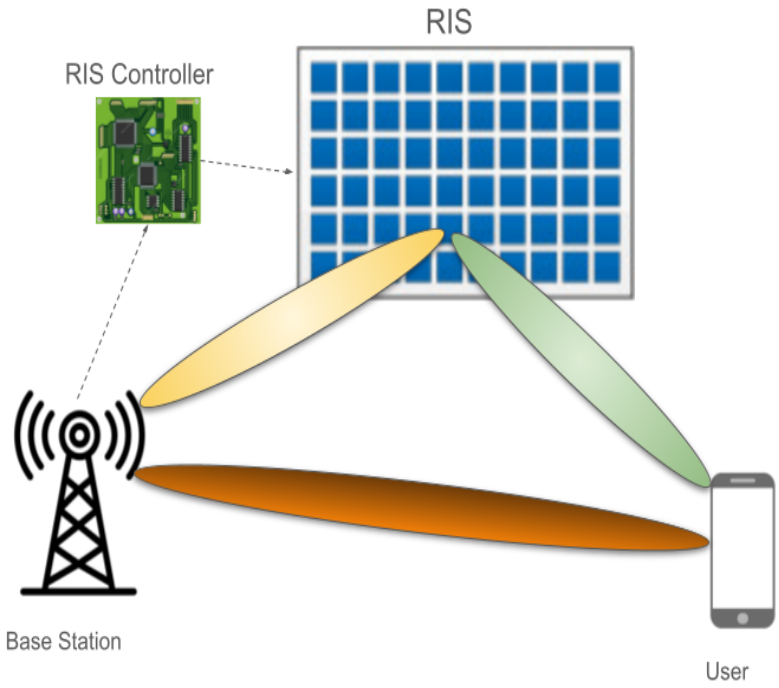

Figure 1.1: Working of RIS.

can be used on a variety of surfaces in the environment, including building facades, ceilings, furnishings, and clothes. RIS are also ecologically benign and satisfy green communication criteria because they are essentially passive and use no more energy than traditional wireless systems. RIS also support full-duplex and full-band com-

munication since they exclusively reflect electromagnetic radiation. They are cheap because they do not require analog-to-digital/digital-to-analog converters or power amplifiers. Furthermore, the power gain of a RIS follows a quadratic scaling rule, as opposed to the linear power scaling equation of a traditional active antenna array.

However, RISs provide significant obstacles to wireless transceiver design, notably in three areas: channel state information (CSI) estimate, passive information transmission, and low-complexity resilient system design. These issues are particular to RIS-aided networks since RIS linkages are cascaded and passive, complicating CSI gathering and necessitating passive information transmission. Understanding the trade-offs between system performance and computational cost is critical for fully realizing the potential of RIS-enabled wireless networks.

1.1.2 Unmanned Aerial Vehicles

Unmanned aerial vehicles (UAV) could expand the flexibility of the RIS by allowing for airborne mobility. UAV is a plane that flies without a driver on board. It improves communication by delivering signals over the air, increasing the base station's range and creating an extra path with spatial variety. It may also provide quick assistance to people on ground level by altering its location in real time. UAVs have been employed for a variety of purposes, including military operations, surveillance, monitoring, telecommunications, medical supplies distribution and rescue missions.

Recent advances in drone technology have enabled the use of UAVs for wireless communications, providing cost-effective and dependable solutions. UAVs can serve as airborne base stations or user devices, improving access to cellular and broadband networks. Their mobility, flexibility, and changeable altitude enable them to supplement traditional base stations by increasing capacity in hotspots and expanding coverage to remote locations.

UAVs play critical roles in IoT settings, operating as relays to improve connection and coverage for ground devices, especially in surveillance. They provide a cost-effective alternative to developing cellular infrastructure, as demonstrated by initiatives such as Google's Loon. Industry leaders such as Qualcomm and AT&T want to use UAVs for extensive wireless communication in 5G networks, while projects such as Amazon Prime Air and Google's Project Wing investigate cellular-connected UAVs [4]. However, attaining their full potential requires overcoming technological

challenges ranging from effective placement and resource allocation to handover management and interference reduction.

Choosing the appropriate type of UAV is critical depending on individual requirements and laws. They are essentially divided into two types based on height: high altitude platforms (HAPs) and low altitude platforms(LAPs). LAPs have a maximum height of 400 feet and are ideal for quick activities such as emergency response and ground data collecting. HAPs have more endurance for prolonged coverage, but they are more expensive and require longer deployment periods. UAVs are also classified as fixed-wing (like airplanes) or rotary-wing (like quadrotors), with each having distinct capabilities and flying characteristics.

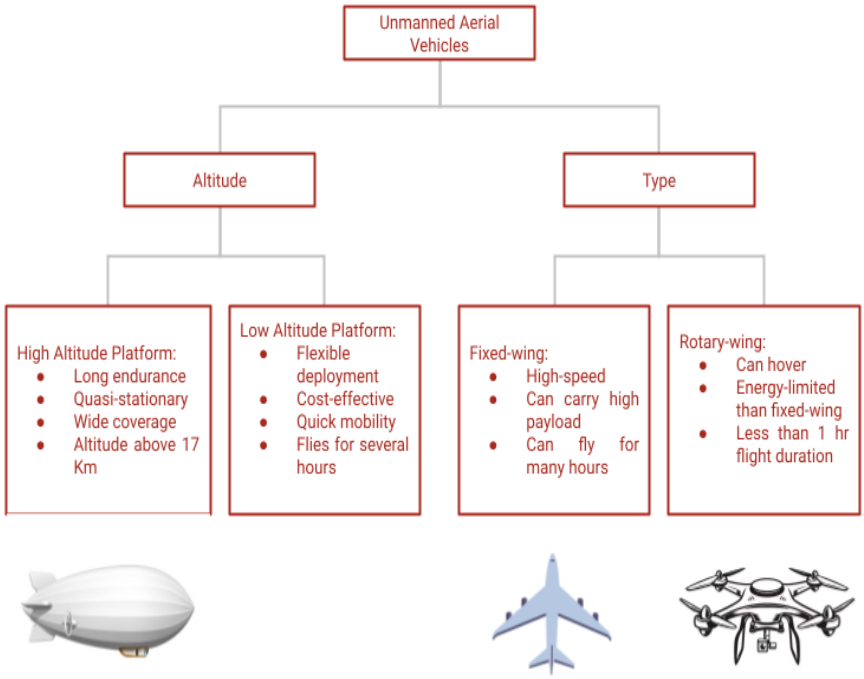

Figure 1.2: UAV Classification.

1.1.3 Non-Orthogonal Multiple Access

Non-orthogonal multiple access (NOMA), a new technique, is intended to be used in this case [5]. NOMA takes an innovative method by enabling many users in the power domain, resulting in a distinct type of multiplexing inside standard time or frequency domains. Unlike traditional multiple access strategies, NOMA is an extra way that may complement current legacy systems while offering improved integration possibilities. It improves spectral efficiency by implementing power-

based multiple access, allowing for effective sharing of spectrum resources among many different users.

This subsection gives a brief review of Superposition Coding (SC) and Successive Interference Cancellation (SIC), two fundamental approaches for understanding power-domain NOMA. SC allows a single transmitter to send information to numerous receivers at once. SC, like a lecturer adapting a presentation to students from various backgrounds, enables each user to obtain information adapted to their specific requirements. In practice, the transmitter encodes information specific to each user via discrete point-to-point encoders that convert inputs to complex-valued sequences. During superposition encoding, point-to-point encoders convert input bits into output sequences. These sequences are then concatenated using a summation device to produce an output sequence.

SIC decodes superposed signals by using signal strength disparities. The approach entails decoding user signals in sequence, with each decoded signal removed from the aggregate signal before decoding the next. Users are sorted according to signal intensity, allowing the receiver to interpret stronger signals first and isolate weaker ones. By using SIC at receivers, users with better channel conditions may efficiently eliminate interference created by users with poorer channels while deciphering the intended messages.

1.1.4 Physical Layer Security

Wireless networks require security because wireless signals are vulnerable to eavesdropping, denial of service (DoS) attacks (defined later) and data fabrication. The most important security criteria are:

- Confidentiality: Only the intended users should have access to confidential data.
- Authenticity: Differentiate between authorized and illegitimate users.
- Availability: Ensure that authorized users have access to wireless network resources whenever and wherever they need them.
- Integrity: Ensure the correctness of delivered information without fabrication.

Wireless networks should provide the same degree of security as wired networks. However, the broadcast nature of wireless communication creates particular obsta-

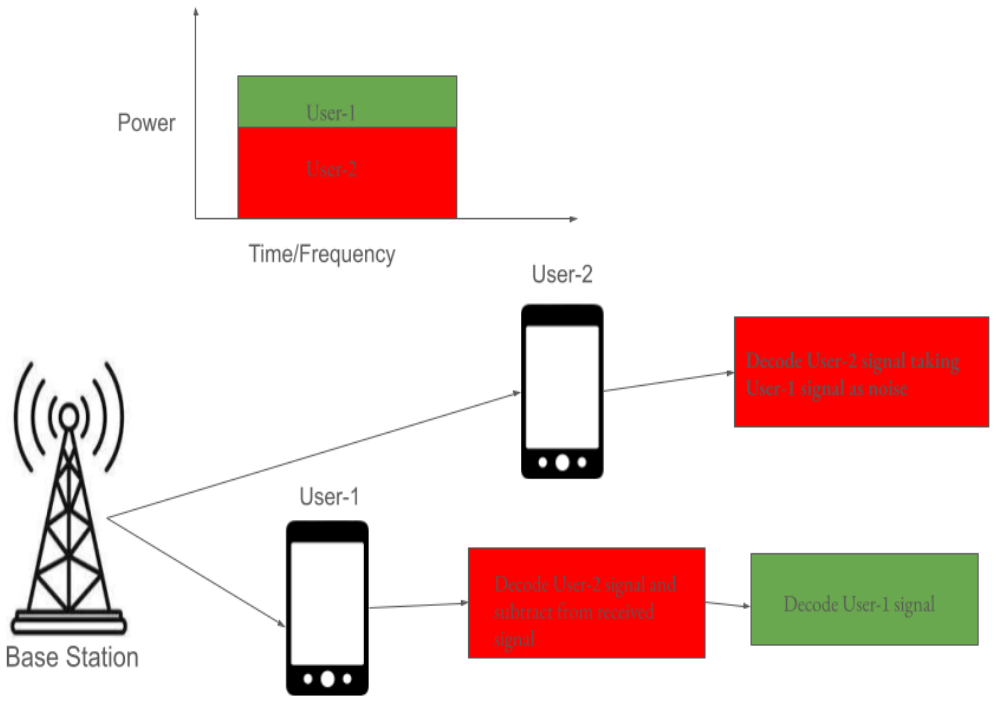

Figure 1.3: Working of NOMA.

cles. For example, wireless networks are more vulnerable to interruptions, such as jammer assaults, which may readily disrupt physical-layer communications. To address such dangers, wireless systems frequently use methods such as DSSS or FHSS in addition to traditional security measures found in wired networks.

Another phenomenon that requires attention are the signal delays that are caused by propagation routes owing to reflection, diffraction, and scattering. They result in multipath effects in which signal components can add or cancel one another. This variation in signal attenuation over time, known as fading, is often described as a random process, which can be increased by barriers that cause shadowing.

Physical-layer security uses wireless channel characteristics to improve security, relying on the idea that the wiretap channel is a degraded version of the main channel. The time-varying nature of wireless channels, combined with random fading discussed above, makes it difficult to provide trustworthy information-theoretic security. As a result, major research efforts have been directed into a variety of physical-layer security approaches.

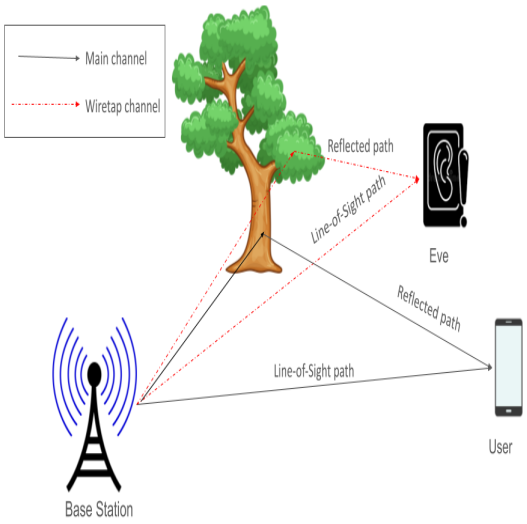

Figure 1.4: Eavesdropper in action.

Jammers

Wireless networks are vulnerable to both eavesdropping and jamming assaults due to the shared nature of radio transmission. Jamming attacks impair lawful wireless communications by sending out unwanted radio frequencies. A jammer's purpose is to prevent legitimate nodes from transmitting or receiving data. Jamming attackers use a variety of techniques to achieve their goals:

- Intermittent jammer: A jamming signal is emitted on a periodic basis.
- Constant jammer: Constantly sends a jamming signal.
- Adaptive jammer: The jamming signal is tailored dependent on the power received by the genuine receiver.
- Reactive jammer: Sends out a jamming signal only when it detects continuous lawful transmissions.
- Intelligent jammer: Uses flaws in upper-layer protocols to prevent genuine transmissions.

The first four types of jammers use the common wireless medium, resulting in physical-layer jamming assaults. Intelligent jammers, on the other hand, seek for flaws in upper-layer protocols. These assaults are commonly referred to as DoS attacks.

Depending on the design, jammers can also assist in interrupting eavesdropper (Eve) transmissions. Considering the physical weight and size limits of UAVs, the significant energy consumption caused by cryptographic algorithms presents a hurdle. Fortunately, including PLS into broadcast system design has come to be a feasible and computationally profitable security measure for UAV-enabled communications.

1.2 Literature Survey

Studies were conducted that combined the use of RIS with UAVs. Yang et al. put a RIS on a building and investigated UAV-based communication for a single user. The results indicated that RIS enhances UAV communication coverage and reliability if total time for service is inadequate. In [8], the researchers examined the functioning of a combined UAV-RIS relay for just one user system. Three different transmission modes were considered: coupled UAV-RIS, RIS-only, and UAV-only. The ideal UAV-RIS height varies depending on the transmission technique. In addition, in most cases, the integrated mode offers the lowest chance of outage.

Integrating NOMA in this system leads in more degree of freedom for efficient resource utilization design than OMA methods, as observed in Y. Cal *et al.* [9], who studied the operation of a fixed-RIS and UAV-based communication for multiple users using NOMA. C. K. Singh et al. [10] studied the functioning of a network containing two users utilizing NOMA after integrating UAV and RIS. Practical concerns such as residual device limitations and imprecise SIC in NOMA were explored, yet NOMA outperformed OMA. They also developed a deep neural network (DNN) model for predicting outage probabilities in a stochastic dynamic context. In [11], the authors evaluated the effectiveness of RIS-assisted aerial communications. This involves a ground base station using NOMA to interact with distant land and airborne users via a RIS-equipped UAV. The study found that NOMA could offer fairness to users under various channel circumstances by properly allocating RIS components.

With the occurrence of an Eve, the PLS component of downlink RIS-assisted NOMA systems was studied in [12]. The RIS was deployed to enhance quality by allowing cell-edge users to communicate with the base station. In [13], Wang et al. investigated the confidentiality capacity of a combined UAV-RIS relay for a single

user with many Eves. Various eavesdropping channels, including independent and cooperative incidents, were explored. In [14], authors analyzed the secrecy outage probability (SOP) of a UAV-aided NOMA system with an Eve. They employed artificial noise delivered from the UAV to avoid eavesdropping.

In [15], H. Yang et al. investigated a RIS-assisted UAV system that had restricted CSI to combat numerous Eves and a malevolent jammer by using transmit beamforming as well as artificial noise. In [16], the employment of jammers to prevent eavesdropping was investigated. A transmitter was used to convey messages to two valid users, while a warden verified the presence of the communication. To disguise the powerful user's broadcast from the warden, a helpful land jammer was successfully deployed.

In [17], Zhou et al. examined the secrecy performance of a terrestrial communication system including Eve and legitimate nodes, as well as a UAV-based jammer. The study examined the performance of mobile and fixed UAV jammers in two different circumstances, revealing that UAV jammers had a substantially longer jamming range than terrestrial jammers. At the same time, [18] investigated outage probability in an IoT system combining NOMA with IoT relays. The system faced a malevolent terrestrial jammer, collaborating Eves, and a UAV operating as a friendly jammer to counterbalance the Eves. Another research by [19] investigated a situation where a UAV functioned as a source for both NOMA users, with an Eve attempting to intercept the connection. They used an aerial jammer to prevent the eavesdropper's interception attempts.

In [20], PLS of a RIS-assisted UAV NOMA system has been studied and it was shown that the positioning of Eve also influences performance. In [21], a safe transmission technique using RIS-aided NOMA was studied, with UAVs equipped with RIS functioning as relays. Using RIS to adapt the geographical distribution of signal strength increased security against Eves. To increase the safe transmission rate, UAV position, NOMA transmit signal strength, and RIS phase shift were all tuned at the same time.

Recent research shows that deep learning (DL) algorithms can successfully handle real-world difficulties in wireless communication networks, such as managing congestion, allocation of resources [22], CSI estimation [23] and beamforming [24]. In [9], authors employed deep learning to properly compute actual channel gains when

design difficulties became intractable. As a result, deep learning will be critical in meeting the increased needs projected in 6G communication settings.

According to the preceding discussion, the benefits of RIS to increase channel strength, NOMA to effectively utilize frequency resources, overhead jammers to block Eve's interception and improve PLS, and UAV that offers aerial mobility and a line-of-sight (LoS) channel with terrestrial nodes are observed. This research investigates the effectiveness of confidentiality of a UAV-aided RIS system where an Eve tries to intercept the NOMA signal carrying the message for both users. The use of an aerial jammer prevents Eve from properly decoding the transmission. Then, to anticipate the SOP in a real-time, high-demanding environment, a deep learning-based model is constructed that predicts quicker than mathematical analysis.

1.3 Motivations and Contributions

The present research examines a UAV-assisted RIS NOMA system in which the base station (BS) supports both a normal and a cell-edge user using NOMA. In this system, the cell-edge user is unable to connect directly to the BS and must instead rely on the UAV-RIS. Eve is thought to be in the best position for capturing the NOMA signal, as it is situated near to the cell-edge user. Interestingly, in this circumstance, the existence of RIS allows both the genuine user and Eve to get a greater signal. Because of this circumstance, including a jammer that is favorable to genuine users helps to mislead Eve while still securing the information. The primary contributions of this thesis are outlined as follows:

- A NOMA-based two-user grouping with a UAV-aided RIS capable of serving a remote user is suggested. The impacts of utilizing the RIS, that is designed to help the remote user, are investigated.

- Major previous research use the theorem of central limit to estimate the RIS channel, assuming there are an adequate amount of RIS elements. To evaluate system performance with fewer reflecting RIS pieces, a realistic Rician channel model is employed to show the aerial path across RIS from its source to the permitted distant user.

- System performance is analyzed using SOP and asymptotic SOP. Secrecy outages depend on features such as power allocation coefficients and the amount

of RIS surface components. The proposed network's performance is compared to other OMA designs.

- A DNN model is created to anticipate SOPs in a dynamic environment, with faster computational times over mathematical analysis as well as Monte-Carlo simulations.

The report is divided into the subsequent chapters. Chapter-2 describes the UAV-RIS NOMA system and channel models, in addition to the way the core signal-to-interference-noise-ratio (SINR) formulae were developed. Chapter-3 thoroughly analyzes the system's performance with SOP and asymptotic SOP. Chapter-4 presents a DNN framework for assessing dynamic system parameters. Chapter-5 gives numerical and simulation results, while Chapter-6 provides conclusions.

CHAPTER 2

SYSTEM MODEL

In this chapter, the system model which will form the basis for rest of the work in this thesis will be presented. The channel conditions faced by the users, jammer, RIS and Eve will be explored. Also the SINR expressions for each user will be derived.

2.1 System Model

Figure 2.1 illustrates the proposed UAV-aided RIS system. The configuration includes a source (S) interacting with the two NOMA users, U_1 as well as U_2 and Eve U_e lurking within its transmission range. In addition, the device has an airborne jammer J to counteract Eve. In comparison to user U_2, U_1 is deemed to be close to the S. Obstacles such as buildings impede the passage between S and U_2, preventing a LoS channel from being established. The user U_1 gets the signal straight from the S through a direct link. The RIS is mounted to a UAV and has N RIS reflective components. This has been placed near U_2 so that the RIS can get CSI values of U_2 and optimize signal power at U_2.

Φ defines the $N \times N$ diagonal phase-shifting matrix at the RIS. Φ = diag $(\beta_1 e^{j\phi_1}, \beta_2 e^{j\phi_2}, \beta_3 e^{j\phi_3}, ...\beta_N e^{j\phi_N})$, wherein $\beta_n \in (0, 1]$ corresponds to the n-th amplitude reflection factor, with $\beta_n = 1$ denoting complete reflection, and $\phi_n \in [0, \pi)$ is the n-th phase-shift parameter. The aerial jammer, hovering near the remote user, seeks to emit a jamming signal that will interfere with Eve's capacity to receive genuine signals. This jamming message is identifiable to the distant user and will have no impact with its capacity to conduct SIC on the signal it has received and decode the needed information.

The node positions are expressed utilizing the three-dimensional in nature, Carte-

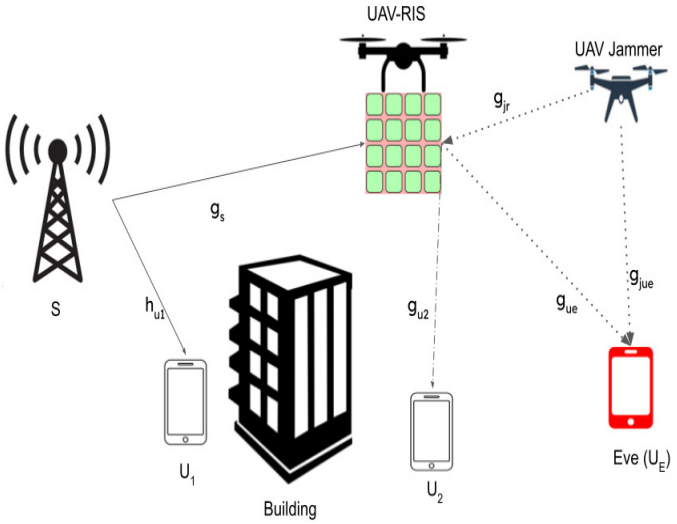

Figure 2.1: System Model

sian coordinates as $l_s = (X_s, Y_s, 0)$, $l_{u_1} = (X_{u_1}, Y_{u_1}, 0)$, $l_{u_2} = (X_{u_2}, Y_{u_2}, 0)$. The UAV-RIS moves at a constant speed along a circular route of radius r_r and height H_r, such that $H_r \in [H_r^{min}, H_r^{max}]$, where H_r^{min} and H_r^{max} are the permitted minimum and maximum altitudes, respectively. Positioning with an angle of ϕ_r to the $\mathcal{X}$-axis inside the UAV-RIS circle. The position is provided as $l_r = (r_r \cos\phi_r, r_r \sin\phi_r, H_r)$. The UAV-RIS is assumed to be stable in relation to the ground, with a set angle from the $\mathcal{X}$-axis and a constant level above ground. Elevation angles from ground nodes S and U_2 (expressed in radians) are determined by $\theta_{rs} = \arctan(\frac{H_r}{|l_r - l_s|})$ and $\theta_{ru_2} = \arctan(\frac{H_r}{|l_r - l_{u_2}|})$.

The aerial jammer is located at $l_j = (r_j \cos\phi_j, r_j \sin\phi_j, H_j)$. where ϕ_j is the angle it makes with regard to the $\mathcal{X}$-axis inside the jammer circle of radius r_j, H_j^{min} and H_j^{max} are the permissible lowest and maximum altitudes for the jammer. The jammer is assumed to be stationary in relation to the ground, with a set angle from the $\mathcal{X}$-axis and an equal height above ground. The elevation tilt measured from the ground node U_2 (shown in radians) is described by $\theta_{ju_2} = \arctan(\frac{H_j}{|l_j - l_{u_2}|})$. The elevation angle from the jammer to the RIS is written as $\theta_{jr} = \arctan(\frac{|H_j - H_r|}{|l_j - l_r|})$.

2.2 Channel Model

The communication links that connect the UAV and ground nodes may be LoS or non-LoS, based on the conditions and elevation angles. The the chance of LoS in

the relevant links is provided by

$$P_L(\theta_i) = (1 + \epsilon_i \exp(-\xi_i(\theta_i - \epsilon_i)))^{-1}, \tag{2.1}$$

where ϵ_i and ξ_i with $i \in \{rs, ru_2, jr, ju_2\}$, indicate the environment parameters obtained from the curve fitting using the Damped Least Squares (DLS) approach [25]. The path-loss exponents for UAV-RIS channels are provided by

$$\alpha_{r,l} = P_L(\theta_{r,l})\kappa_{r,l} + \upsilon_{r,l}, \tag{2.2}$$

where κ_l and υ_l with $l \in \{s, u_2\}$ represent constants that are dependent on the uplink and downlink circumstances.

The path-loss exponent for the aerial jammer channel is provided as

$$\alpha_{j,l} = P_L(\theta_{j,l})\kappa_{j,l} + \upsilon_{j,l}, \tag{2.3}$$

where κ_l and υ_l with $l \in \{r, u_2\}$ signify values that depend on the uplink and downlink environment. α_{su_1} represents the route loss encountered by a signal going from S to U_1 over the terrestrial channel.

The distances that exist among S and U_1 (d_{su_1}), S and UAV-RIS (d_{sr}), UAV-RIS and U_2 (d_{ru_2}), and airborne jammer to UAV-RIS (d_{jr}) are as follows,

$$d_{su_1} = \sqrt{|X_{u_1} - X_s|^2 + |Y_{u_1} - Y_s|^2}, \tag{2.4}$$

$$d_{sr} = \sqrt{|r_r \cos\phi_r - X_s|^2 + |r_r \sin\phi_r - Y_s|^2 + H_r^2}, \tag{2.5}$$

$$d_{ru_2} = \sqrt{|r_r \cos\phi_r - X_{u_2}|^2 + |r_r \sin\phi_r - Y_{u_2}|^2 + H_r^2}, \tag{2.6}$$

$$d_{jr} = \sqrt{|R_c|^2 + |R_s|^2 + |H_j - H_r|^2}, \tag{2.7}$$

where $R_c = r_j \cos\phi_j - r_r \cos\phi_r$ and $R_s = r_j \sin\phi_j - r_r \sin\phi_r$.

The $N \times 1$ aerial channel vector among S and UAV-RIS is represented by $\mathbf{g_s}$. The link between S and U_1 is represented by h_{u_1}. The links that connect the UAV-RIS and U_2, the jammer and UAV-RIS, the UAV-RIS and U_e and the aerial jammer and U_e are denoted as $\mathbf{g_{u_2}}$, $\mathbf{g_{jr}}$, $\mathbf{g_{u_e}}$ and $\mathbf{g_{ju_e}}$, respectively.

Since the UAV-RIS is usually deployed at a location with LoS to S, U_2 and J, it is attractive to use the Rician fading model for $\mathbf{g_s}, \mathbf{g_{u_2}}$ and $\mathbf{g_{jr}}$ as $\mathbf{g_i} = \sqrt{\frac{K_i}{K_i+1}}\bar{\mathbf{g}}_\mathbf{i} +$

$\sqrt{\frac{1}{K_i+1}}\tilde{\mathbf{g}}_\mathbf{i}$. Here, K_i denotes the Rician factor, $\bar{\mathbf{g}}_\mathbf{i}$ and $\tilde{\mathbf{g}}_\mathbf{i}$ represent the normalized LoS and non-LoS components, respectively. It is assumed that Ω_i is the average power of the corresponding Rician channel gain for $i \in \{s, u_2, jr\}$. Because there is no LoS route between S and U_1, it is assumed that the terrestrial in nature channel parameter h_{u_1}, defined as $\mathcal{CN}\left(0, \frac{1}{2\Omega_{su_1}^2}\right)$, undergoes Rayleigh fading.

2.3 Signal Model

Employing NOMA, the S applies a combination of the unit-power message signals x_1 and x_2 for the targeted recipients U_1 and U_2, respectively, with corresponding power factor allocations a_1 and a_2 matching the conditions $a_1 < a_2$ and $a_1 + a_2 = 1$. The total message signal is provided by

$$x_s = \sqrt{a_1 P_s} x_1 + \sqrt{a_2 P_s} x_2, \tag{2.8}$$

where P_s is the transmitted power of S. The signal that is obtained by U_1 through the direct connection is provided by

$$y_{u_1} = b_1 h_{u_1} x_s + \nu_{u_1}, \tag{2.9}$$

where $b_1 = \sqrt{d_{su_1}^{-\alpha_{su_1}}}$ and ν_{u_1} represents the additive white gaussian noise (AWGN) at U_1, represented as $\mathcal{CN}(0, \sigma^2)$.

The signal obtained by U_2 via the UAV-RIS link is supplied by

$$y_{u_2} = b_2 (g_{u_2}^H \Phi g_s) x_s + \nu_{u_2}, \tag{2.10}$$

where $b_2 = \sqrt{d_{sr}^{-\alpha_{sr(\theta_{sr})}}} \sqrt{d_{ru_2}^{-\alpha_{ru_2(\theta_{ru_2})}}}$ and ν_{u_2} represents AWGN at U_2 modeled as $\mathcal{CN}(0, \sigma^2)$.

The signal received by U_e is given as

$$y_{u_e} = b_2 (g_{u_e}^H \Phi g_s) x_s + \left(b_{j_1} (g_{u_e}^H \Phi g_{jr}) + b_{j_2} g_{ju_e} \right) \sqrt{P_j} x_j + \nu_{u_e}, \tag{2.11}$$

where $b_{j_1} = \sqrt{d_{jr}^{-\alpha_{jr(\theta_{jr})}}} \sqrt{d_{ru_2}^{-\alpha_{ru_2(\theta_{ru_2})}}}$, $b_{j_2} = \sqrt{d_{ju_2}^{-\alpha_{ju_2(\theta_{ju_2})}}}$ and ν_{u_e} represents AWGN at U_e modeled as $\mathcal{CN}(0, \sigma_e^2)$.

2.3.1 SINRs at Users

U_1 interprets the message x_2 of U_2 first, so that x_1 can be deciphered after being cancelled from the incoming signal. So, the SINR at U_1 is specified as

$$\gamma_{u_1}^{x_2} = \frac{a_2 P_s b_1^2 |h_{u_1}|^2}{a_1 P_s b_1^2 |h_{u_1}|^2 + \sigma^2}. \tag{2.12}$$

After removing x_2 using SIC, U_1 decodes its own message, x_1. The requisite signal-to-noise ratio (SNR) is supplied by

$$\gamma_{u_1}^{x_1} = \frac{a_1 P_s b_1^2 |h_{u_1}|^2}{\sigma^2}. \tag{2.13}$$

Consider $\beta_n = \beta = 1 \, \forall \, n$ at U_2, without compromising generality, and supposing that $g_{s,n}$ and $g_{u_2,n}$ correspond to the n-th elements of g_s and g_{u_2}, respectively. Using the derived ideal CSI $\psi_{s,n}$ of $g_{s,n}$ and $\psi_{u_2,n}$ of $g_{u_2,n}$, the RIS can modify the phase shift element ϕ_n as $\phi_n = \psi_{s,n} + \psi_{u_2,n}$, allowing the received signal to be represented as

$$y_{u_2} = b_2(\tilde{g}_{u_2}) x_s + \nu_{u_2}, \tag{2.14}$$

where $\tilde{g}_{u_2} = \sum_{n=1}^{N} |g_{u_2,n}||g_{s,n}|$. Here, U_2 can decipher its own message x_2 while treating x_1 as noise. The matching SINR is shown as

$$\gamma_{u_2}^{x_2} = \frac{a_2 P_s b_2^2 |\tilde{g}_{u_2}|^2}{a_1 P_s b_2^2 |\tilde{g}_{u_2}|^2 + \sigma^2}. \tag{2.15}$$

In Eve U_e, the most severe situation for a RIS-aided NOMA network is examined, where Eve lies inside the beam cone and all S-RIS-Eve signals are co-phased [12]. Eve is thought to have good detection skills and can recognize messages from the associated NOMA users. In light of this assumption, the lower limit of secrecy performance for the given system will be determined. As a consequence, the related channel of U_e is the same as User 2's channel, and may be described as $\tilde{g}_{u_e} = \sum_{n=1}^{N} |g_{u_e,n}||g_{s,n}|$.

Consider the other link traveling via the UAV-RIS, namely the Jammer-RIS-Eve channel, whose channel coefficient is indicated as $g_{jre} = (g_{u_e}^H \Phi g_{jr}) = \sum_{n=1}^{N} |g_{u_e,n}||g_{jr,n}| e^{j\phi_n}$ [16]. If the RIS phase adjustments are at random, the theorem of central limit can be used to streamline the process. For $x > 0$, the PDF and CDF of $|g_{jre}|^2$ are

$f_{|g_{jre}|^2}(x) = \frac{e^{-\frac{x}{N}}}{N}$ and $F_{|g_{jre}|^2}(x) = 1 - e^{-\frac{x}{N}}$, accordingly.

The SNR to identify x_1 and x_2 by U_e is

$$\gamma_{u_e}^{x_i} = \frac{a_i P_s b_3^2 |\tilde{g}_{u_e}|^2}{P_j (b_{j_1}|g_{jre}| + b_{j_2}|g_{ju_e}|)^2 + \sigma_e^2}. \tag{2.16}$$

By considering $\Lambda_e = b_{j_1}|g_{jre}| + b_{j_2}|g_{ju_e}|$, the above SNR can be rewritten as

$$\gamma_{u_e}^{x_i} = \frac{a_i \rho_e b_3^2 |\tilde{g}_{u_e}|^2}{\rho_j (\Lambda_e)^2 + 1}, \tag{2.17}$$

where $\rho_e = \frac{P_s}{\sigma_e^2}$ and $\rho_j = \frac{P_j}{\sigma_e^2}$. For simplicity, ρ_s is used, where $\rho_s = \frac{P_s}{\sigma^2}$.

CHAPTER 3

PERFORMANCE ANALYSIS

This chapter analyzes the performance of the suggested system by directly developing SOP expressions for users U_1 and U_2. The asymptotic SOP is then calculated to acquire a better understanding of the system.

Lemma 1: The cumulative distribution function of γ_{u_1} is

$$F_{\gamma_{u_1}}(x) = \begin{cases} 1 - e^{\frac{-x}{a_1 b_1^2 \rho_s \Omega_{su_1}}}, & \text{if } 0 < x < \dfrac{a_2}{a_1} - 1, \\ 1 - e^{\frac{-x}{(a_2 - a_1 x) b_1^2 \rho_s \Omega_{su_1}}}, & \text{if } \dfrac{a_2}{a_1} - 1 < x < \dfrac{a_2}{a_1}, \\ 1, & \text{if } x > \dfrac{a_2}{a_1}. \end{cases} \tag{3.1}$$

Proof:

$$\begin{aligned} & F_{\gamma_{u_1}}(x) = Pr\{\gamma_{u_1}^{x_2} < x \text{ or } \gamma_{u_1}^{x_2} < x\} \\ & = 1 - Pr\{\gamma_{u_1}^{x_2}, \gamma_{u_1}^{x_2} > x\} \\ & = 1 - Pr\left\{|h_{u_1}|^2 > \max\left(\frac{x}{(a_2 - x a_1)\rho_s b_1^2}, \frac{x}{a_1 \rho_s b_1^2}\right)\right\} \\ & = \begin{cases} 1 - \Pr\left\{|h_{u_1}|^2 > \frac{x}{a_1 \rho_s b_1^2}\right\}, & \text{if } 0 < x < \frac{a_2}{a_1} - 1, \\ 1 - \Pr\left\{|h_{u_1}|^2 > \left(\frac{x}{(a_2 - x a_1)\rho_s b_1^2}\right)\right\}, & \text{if } \frac{a_2}{a_1} - 1 < x < \frac{a_2}{a_1}, \\ 1, & \text{if } x > \frac{a_2}{a_1}. \end{cases} \end{aligned} \tag{3.2}$$

Using the exponential distribution as the CDF, followed by $|h_{u_1}|^2$, the CDF is pro-

duced.

Remark: For $x > \frac{a_2}{a_1}$, the CDF hits one, suggesting a ceiling effect.

Lemma 2: The CDF of γ_{u_2} is given by

$$F_{\gamma_{u_2}}(x) = \begin{cases} \dfrac{\gamma\left\{\kappa_2 + 1, \sqrt{\dfrac{x}{(a_2 - a_1 x) b_2^2 \rho_s \theta_2^2}}\right\}}{\Gamma(\kappa_2 + 1)}, & \text{if } 0 < x < \dfrac{a_2}{a_1}, \\ 1, & \text{if } x > \dfrac{a_2}{a_1}, \end{cases} \tag{3.3}$$

where $\kappa_2 = \frac{NE\{|g_{u_2,n}||g_{s,n}|\}^2}{Var\{|g_{u_2,n}||g_{s,n}|\}} - 1$, $\theta_2 = \frac{Var\{|g_{u_2,n}||g_{s,n}|\}}{E\{|g_{u_2,n}||g_{s,n}|\}}$, $N =$ number of RIS elements,

$$\begin{aligned} E\{|g_{u_2,n}||g_{s,n}|\} = &\left[(K_1+1) I_0\left(\frac{K_1}{2}\right) + K_1 I_1\left(\frac{K_1}{2}\right)\right] \\ &\times \left[(K_2+1) I_0\left(\frac{K_2}{2}\right) + K_2 I_1\left(\frac{K_2}{2}\right)\right] \\ &\times \frac{\pi e^{\frac{(-K_1-K_2)}{2}}}{4\sqrt{\Omega_1 \Omega_2}}, \end{aligned} \tag{3.4}$$

$$Var\{|g_{u_2,n}||g_{s,n}|\} = \frac{(K_1+1)(K_2+1)}{\Omega_1 \Omega_2} - E\left\{|g_{u_2,n}||g_{s,n}|\right\}^2. \tag{3.5}$$

The Rician parameters for the channel g_s are K_1, Ω_1, whereas K_2, Ω_2 are for the channel g_{u_2}.

Proof: With regard to [26], the CDF of SNR γ of a RIS-assisted link under Rician fading model is stated as

$$\gamma = \bar{\gamma} \sum_{l=1}^{N} |a_l||b_l| = \bar{\gamma} \sum_{l=1}^{N} R_l^2 \tag{3.6}$$

$$F_\gamma(x) = \frac{\gamma\left(\hat{a} + 1, \frac{\sqrt{x}}{\hat{b}\sqrt{\bar{x}}}\right)}{\Gamma(\hat{a} + 1)} \tag{3.7}$$

where $\bar{\gamma} =$ average SNR $= \dfrac{P_s}{N_o}$, $\hat{a} = \frac{NE(R_l)^2}{Var(R_l)} - 1$, $\hat{b} = \frac{Var(R_l)}{E(R_l)}$.

Applying the aforementioned CDF to γ_{u_2} yields the following:

$$F_{\gamma_{u_2}}(x) = Pr\{\gamma_{u_2}^{x_2} < x\} = Pr\left\{\tilde{g}_{u_2} < \frac{x}{(a_2 - a_1 x)b_2^2\rho_s}\right\}$$
$$= \frac{\gamma\left(\kappa_2 + 1, \frac{\sqrt{\frac{x}{(a_2 - a_1 x)b_2^2\rho_s}}}{\theta_2}\right)}{\Gamma(\kappa_2 + 1)} \tag{3.8}$$

Remark: Similar to User-1, when $x > \frac{a_2}{a_1}$, the CDF hits 1, suggesting a ceiling effect.

3.1 Secrecy Outage Probability Analysis

In this network, the capacity of the main channel of the i-th user is provided by $C_{u_i} = \log(1+\gamma_{u_i})$ and the capacity of Eve's channel for the i-th user is represented as $C_{u_{e_i}} = \log(1+\gamma_{u_{e_i}})$. The secrecy rate for the i-th user is given as $C_i = [C_{u_i} - C_{u_{e_i}}]^+$. At the i-th user, if $C_{u_i} < R_{th}$, in which R_{th} is the rate at which data is transferred, the SOP is stated as $P_i(R_{th}) = Pr\{C_{u_i} < R_{th}\}$. The SOP for User-1 therefore becomes

$$P_1(R_{th}) = Pr\{C_{u_1} < R_{th}\}$$
$$= Pr\left\{\left(\log_2^{(1+\gamma_{u_1})} - \log_2^{(1+\gamma_{u_{e_1}})}\right)^+ < R_{th}\right\}$$
$$= F_{\gamma_{u_1}}\left(2^{R_{th}} + 2^{R_{th}}(E\{\gamma_{u_{e_1}}\}) - 1\right)$$
$$= \begin{cases} 1 - e^{\frac{-\hat{x_1}}{a_1 b_1^2 \rho_s \Omega_{su_1}}}, & \text{if } 0 < \hat{x_1} < \frac{a_2}{a_1} - 1, \\ 1 - e^{\frac{-\hat{x_1}}{(a_2 - a_1\hat{x_1})b_1^2\rho_s\Omega_{su_1}}}, & \text{if } \frac{a_2}{a_1} - 1 < \hat{x_1} < \frac{a_2}{a_1}, \\ 1, & \text{if } \hat{x_1} > \frac{a_2}{a_1}, \end{cases} \tag{3.9}$$

where $\hat{x_1} = 2^{R_{th}} + 2^{R_{th}}(E\{\gamma_{u_{e_1}}\}) - 1$.

Similar to User-1, the SOP of User-2 is given by:

$$\begin{aligned} P_2(R_{th}) &= Pr\{C_{u_2} < R_{th}\} \\ &= F_{\gamma_{u_2}}(2^{R_{th}} + 2^{R_{th}}(E\{\gamma_{u_{e_2}}\}) - 1 \\ &= \begin{cases} \dfrac{\gamma\left\{\kappa_2 + 1, \sqrt{\dfrac{\hat{x_2}}{(a_2 - a_1\hat{x_2})b_2^2\rho_s\theta_2^2}}\right\}}{\Gamma(\kappa_2 + 1)}, & \text{if } 0 < \hat{x_2} < \dfrac{a_2}{a_1}, \\ 1, & \text{if } \hat{x_2} > \dfrac{a_2}{a_1}, \end{cases} \end{aligned} \tag{3.10}$$

where $\hat{x_2} = 2^{R_{th}} + 2^{R_{th}}(E\{\gamma_{u_{e_2}}\}) - 1$.

Lemma 3: The expectation of SNR of Eve $\gamma_{u_{e_i}}$ is given by

$$E\{\gamma_{u_{e_i}}\} = \mu_{e_i} = \frac{a_i\rho_e b_3^2\theta_e^2\Gamma(\kappa_2 + 3)}{(\rho_j\lambda_e + 1)\Gamma(\kappa_2 + 1)} \tag{3.11}$$

where $\lambda_e = b_{j1}N + b_{j2}$.

Proof: Since, $E\{x\} = \int_0^\infty xf(x)dx$, the CDF and PDF of $\gamma_{u_{e_i}}$ can be found using

$$\begin{aligned} Pr\{\gamma_{u_e}^{x_i} < x\} &= Pr\left\{\frac{a_i\rho_e b_3^2|\tilde{g}_{u_e}|^2}{\rho_j(\Lambda_e)^2 + 1} < x\right\}, \\ &= Pr\left\{(\tilde{g}_{u_e})^2 < \frac{(\rho_j(\Lambda_e)^2 + 1)x}{a_i\rho_e b_3^2}\right\}, \\ &= F_{\tilde{g}_{u_e}^2}\left(E\left\{\frac{(\rho_j(\Lambda_e)^2 + 1)x}{a_i\rho_e b_3^2}\right\}\right), \\ &= F_{\tilde{g}_{u_e}^2}\left(\frac{(\rho_j E\{(\Lambda_e)^2\} + 1)x}{a_i\rho_e b_3^2}\right). \end{aligned} \tag{3.12}$$

Applying the central limit theorem to $\Lambda_e = b_{j_1}|g_{jre}| + b_{j_2}|g_{ju_e}|$. According to [20], Λ_e^2 may be estimated as an exponential distribution with the parameter $\lambda_e = b_{j1}N + b_{j2}$. Substitute this value into the above equation to get

$$F_{\gamma_{u_{e_i}}}(x) = F_{\tilde{g}_{u_e}^2}\left(\frac{(\rho_j\lambda_e + 1)x}{a_i\rho_e b_3^2}\right) \tag{3.13}$$

Eve's channel is equal to User-2's, hence the CDF and PDF of the coefficients of the channel will be the same. The PDF for $\gamma_{u_{e_i}}$ will be

$$f_{\gamma_{u_{e_i}}}(x) = f_{\tilde{g}_{u_e}^2}\left(\frac{(\rho_j\lambda_e + 1)x}{a_i\rho_e b_3^2}\right). \tag{3.14}$$

According to [26], the PDF of $\tilde{g}_{u_e}^2$ will be equal to

$$f_\gamma(x) = \frac{x^{\left(\frac{a-1}{2}\right)} \exp\left(\frac{-\sqrt{x}}{b\sqrt{\bar{x}}}\right)}{2b^{(a+1)}\Gamma(a+1)\bar{x}^{\left(\frac{a+1}{2}\right)}}. \tag{3.15}$$

Then, the PDF of $\gamma_{u_{e_i}}$ becomes

$$f_{\gamma_{u_{e_i}}}(x) = \frac{\left(\frac{\rho_j\lambda_e+1}{a_i\rho_e b_3^2}\right)^{\frac{\kappa_2+1}{2}} \exp\left(-\sqrt{\frac{(\rho_j\lambda_e+1)x}{a_i\rho_e b_3^2\theta_2^2}}\right) x^{\left(\frac{\kappa_2-1}{2}\right)}}{2\theta_2^{\kappa_2+1}\Gamma(\kappa_2+1)}. \tag{3.16}$$

Then,

$$\begin{aligned} E\{\gamma_{u_{e_i}}\} &= \int_0^\infty x f_{\gamma_{u_{e_i}}}(x)dx \\ &= \int_0^\infty \frac{\left(\frac{x(\rho_j\lambda_e+1)}{a_i\rho_e b_3^2}\right)^{\frac{\kappa_2+1}{2}} \exp\left(-\sqrt{\frac{(\rho_j\lambda_e+1)x}{a_i\rho_e b_3^2\theta_e^2}}\right)}{2\theta_e^{\kappa_2+1}\Gamma(\kappa_2+1)}dx. \end{aligned} \tag{3.17}$$

Solving this integral yields the expression stated in the Lemma.

3.2 Asymptotic SOP Analysis

To explain how the network performs under high-SNR situations, asymptotic SOP formulas for users U_1 and U_2 are needed. The transmit SNR for paired NOMA users is considered to be high enough (i.e., $\rho_s \to \infty$), whereas the SNR for the S-RIS-Eve connections is chosen freely. [12] describes the secrecy diversity order as:

$$d_s = -\lim_{\rho\to\infty} \frac{\log P^\infty}{\log \rho_s} \tag{3.18}$$

Corollary-1: The asymptotic SOP of User-1 is given by

$$P_1^\infty(R_{th}) = \begin{cases} \dfrac{\hat{x_1}}{a_1 b_1^2 \rho_s \Omega_{su_1}}, & \text{if } 0 < \hat{x_1} < \dfrac{a_2}{a_1} - 1, \\ \dfrac{\hat{x_1}}{(a_2 - a_1\hat{x_1})b_1^2\rho_s\Omega_{su_1}}, & \text{if } \dfrac{a_2}{a_1} - 1 < \hat{x_1} < \dfrac{a_2}{a_1}. \end{cases} \tag{3.19}$$

Proof: Expanding the exponential function obtained from (3.9) and getting the highest order term produces the equation shown above.

Remark: Substituting (3.18) into (3.19) yields a secrecy diversity order of 1.

Corollary-2: The asymptotic SOP of User-2 is given by

$$P_2^{\infty}(R_{th}) = \sum_{l=0}^{\infty} \frac{(-1)^l \left(\frac{\hat{x_2}}{(a_2 - a_1 \hat{x_2}) b_2^2 \rho_s \theta_2^2} \right)^{\left(\frac{\kappa_2+1+l}{2}\right)}}{l!(\kappa_2 + 1 + l)\Gamma(\kappa_2 + 1)}. \tag{3.20}$$

Proof: Using the lower incomplete Gamma function expansions [[27], (8.354.1)] in (3.10), the aforementioned expression may be obtained.

Remark: Substituting (3.18) into (3.20) and taking the highest order term yields $\frac{\kappa_2 + 1}{2}$ as the secrecy diversity order for User 2.

Given the assumption of perfect SIC for the partnered NOMA users and Eve's strong detecting abilities, the secrecy outages of User 1 and User 2 are treated separately in this situation. As a result, the network's SOP is identified as being related to either User 1 or User 2's outage. Using [12], the entire system's overall system SOP can be found.

$$P_{ov}(R_{th}) = P_1(R_{th}) + P_2(R_{th}) - (P_1(R_{th}) \times P_2(R_{th})). \tag{3.21}$$

CHAPTER 4

DEEP NEURAL NETWORK DESIGN

4.1 Motivation

The deployment of machine learning (ML) in wireless communications can be focused on the network's ability to manage massive volumes of information from its devices and to constantly learn from its environment. The goal is to analyze and anticipate wireless user settings as well as network's environmental circumstances, allowing for data-driven choices in network-wide operations. Also, it may then intelligently regulate and improve its assets based on the information gathered about its wireless surroundings and the current state of its users.

The incorporation of machine learning in wireless networks is becoming increasingly vital for future improvements. ML-driven designs are projected to bring a slew of new network functions and services. While 5G networks may not fully utilize ML, future 6G networks are expected to heavily include ML methods. This is demonstrated by recent moves by companies like Qualcomm and Huawei, who advocate towards smart wireless networks. As a result, the debate has switched from whether machine learning will be utilized in wireless systems to when.

Recent wireless networking ideas, such as context-aware networking, mobile edge caching, and mobile edge computing, have already used machine learning to evaluate user behavior and distribute resources. Deep neural networks (DNNs) are very successful in this area. They often analyze high-dimensional input data, identify representations with low dimensions known as features, and make conclusions based on those characteristics. DNNs are more adept at learning highly complicated func-

tions than shallow artificial neural networks.

This research covers the creation of a DNN system that predicts users' SOP with little delay and high accuracy, enabling efficient performance forecasting without the need for mathematical derivations. This chapter offers a method for calculating SOP with cheap processing costs and a quick run time, which replaces effort-consuming Monte-Carlo simulations and mathematical evaluation.

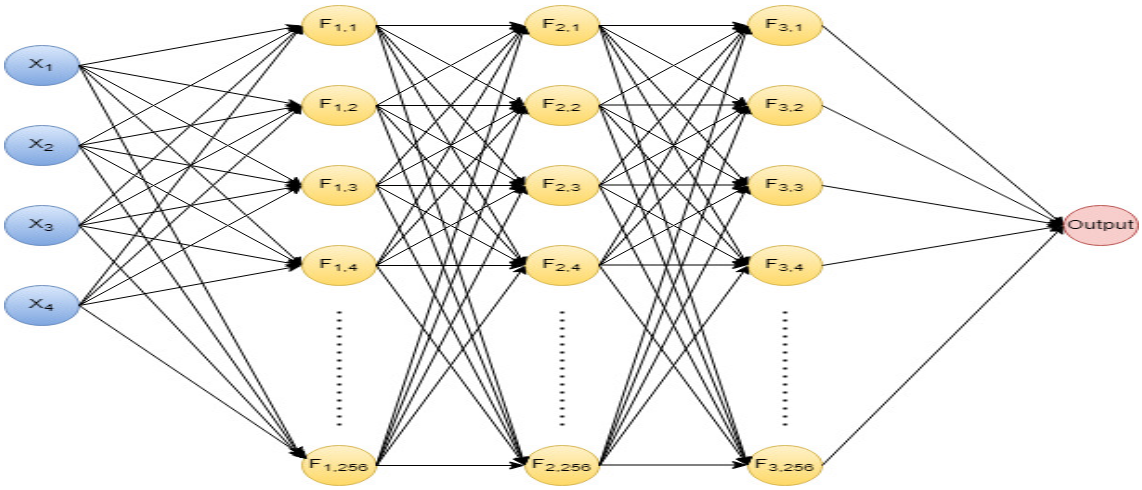

Figure 4.1: DNN Model Architecture.

4.2 Method for Generating Datasets

The dataset for this study is generated by applying the SOP functions in (3.9) and (3.10, which are related to network variables like SNR ($\rho_s \in [10, 60]$), desired rate ($R_{th} \in [0.1, 4]$), the power factor ($a_1 \in [0.01, 0.50]$) and reflecting elements ($N \in [1, 30]$). Every system parameter is built evenly depending on network size and used as a parameter of input during training. The dataset D for each user contains 1.3×10^6 samples, with 60% used for training (D_{trn}) and 40% split equally amongst validation (D_{val}) and testing (D_{tes}). Outliers are eliminated to achieve reliable forecasts.

4.3 Training Process and Learning Model for DNN

Figure-4.1 shows the DNN structure, outlining the procedures for training, validating, testing, and forecasting a DNN model. The DNN architecture includes the following steps:

1) *Data preprocessing:* Normalize the baseline data such that every set has comparable characteristics. The obtained data sets may have various dimensions and units. Standardizing the DNN model's characteristics increases both accuracy and training time.

2) *Training and validating the DNN model:* Verification datasets are employed to continually adjust hyperparameters in order to attain more precise black-box target functions. The DNN model learns the black-box objective function with the use of training data.

3) *Testing the DNN model*: Testing samples evaluate the model's performance following training. The DNN model's effectiveness is measured using RMSE, which is a predictive accuracy metric. The RMSE measurement matches the real data, making it easy to compare the model's accuracy to other measures.

4) *Predicting the DNN model*: Determines if the input matrix matches the input formation for the set of parameters. The created DNN model then accurately identifies the system's SOP.

The feed-forward neural network investigated here contains one input layer, a single output layer, and three hidden layers. The input layer and buried layers each include 256 neurons. The four values provided in the input layer match those given in Section 4.2. Each hidden layer uses the exponential linear unit (eLU) activating function to apply a threshold operation to each input parameter m. Values below zero are increased to zero. This function is described as follows

$$eLU(m) = \begin{cases} e^m - 1, & \text{if } m < 0, \\ m, & \text{if } m \geq 0. \end{cases} \tag{4.1}$$

In a fully connected layer, the activation of the $(p-1)^{th}$ layer is related to the activation $\mathcal{F}_q^p$ of the q-th neuron in the p-th layer as

$$\mathcal{F}_q^p = eLU(\Sigma_{i=1}^{\mathcal{U}_{p-1}} \mathcal{W}_{q,i}^p \mathcal{F}_i^{p-1} + \mathcal{B}_q^p), \tag{4.2}$$

where $\mathcal{U}_{p-1}$ represents the total amount of neurons in the $(p-1)^{th}$ layer. $\mathcal{B}_q^p$ is a scalar bias in the $(p-1)^{th}$ layer, whereas $\mathcal{W}_{q,i}^p$ is the weight related with the i^{th} neuron.

Due to its near-linearity, the activation function of eLU works better than other

activation functions. This regression problem forecasts numerical values directly, which results in a single neuron in the outcome layer.

SOP Real-Time Prediction

The DNN structure consists of two phases: learning and forecasting. The adaptive moment estimation (Adam) optimization approach uses datasets to improve parameters for offline neural network training and input-output correlation learning. During backpropagation, Adam estimates and modifies the DNN model's weights and biases. $\mathcal{M}^d$ and $\bar{\mathcal{M}}^d$ represent the actual and anticipated output values of the DNN model's d^{th} testing samples. The difference in root mean square error (RMSE) between estimated and forecasted values is calculated using the loss function shown below.

$$RMSE(\mathcal{M}^d, \bar{\mathcal{M}}^d) = \sqrt{\frac{\Sigma_{d=1}^{\mathcal{D}_{tes}} (\mathcal{M}^d - \bar{\mathcal{M}}^d)^2}{\mathcal{D}_{tes}}}, \tag{4.3}$$

where $\mathcal{D}_{tes}$ denotes the total number of samples in the testing set.

The calculated DNN model contains about 199k (199,169) parameters.

CHAPTER 5

NUMERICAL AND SIMULATION RESULTS

Monte-Carlo simulations are used to validate the analytical models' correctness. The parameters set in the system are $l_s = (40, 10, 0)$ m, $l_{u_1} = (40, 13, 0)$ m, $l_{u_2} = (10, 20, 0)$ m, $r_r = 20$ m, $H_r = 20$ m, $\phi_r = 0$, $r_j = 5$ m, $H_j = 15$ m, $\phi_j = 0, \Omega_{su_1} = 2, \epsilon_{rs} = \epsilon_{ru_2} = \epsilon_{jr} = \epsilon_{ju_2} = 2, \xi_{rs} = \xi_{ru_2} = \xi_{jr} = \xi_{ju_2} = 1, \alpha_{su_1} = 1.5, \kappa_{rs} = \kappa_{ru_2} = \kappa_{jr} = \kappa_{ju_2} = -1.5, \upsilon_{rs} = \upsilon_{ru_2} = \upsilon_{jr} = \upsilon_{ju_2} = 2, K_s = K_{u_2} = 1$ and $\Omega_s = \Omega_{u_2} = 0.8$. The threshold rates shown in all of the figures are measured in bps/Hz.

TensorFlow 2.15.0 and Python 3.10.12 are utilized to build a DNN model with three hidden layers and 256 neurons hidden per layer. Over 100 training epochs, the DNN's weights are randomly set using the Adam optimizer with a gradient decaying value of 0.95. The learning rate starts at 0.001 and decreases to 90% after 10 epochs. All of the testing was carried out on a PC with an i7-3770 processor and 12 GB of RAM.

Figure-5.1 shows that for U_1, U_2 and the system, lower threshold rates result in greater SOP performance than higher threshold rates. Asymptotic performance is achieved at low SNR in the close user situation, demonstrating that U_1 channel conditions are superior even at low SNR levels. Figure-5.2 shows that when the power allocation coefficient is dropped to the threshold boundaries, the SOP performance worsens for U_1, U_2 and the system.

Figure-5.3 illustrates how increasing the amount of RIS elements affects the SOP for varied SNR for the entire system. In all circumstances, increasing SNR causes a drop in SOP. Overall, the system mimics U_2 performance in the lower part of the SNR range while following U_1 SOP performance in the higher half. The point at

which all the plots merge is evident owing to limited power allocation and the lack of RIS in the channel connection of S to U_1, resulting in no change in the SOP when the amount of RIS components is adjusted. However, having RIS causes a greater reduction of SOP in U_2. It is observed that introducing more RIS parts reduces the likelihood of a secrecy outage. This suggests that the RIS has an influence on increasing SOP performance in the high SNR regime. U_1 performance defines the total system's lowest limit, regardless of how many RIS pieces are attached.

Figure-5.4 depicts the fluctuation of SOP in response to changes in power allocation coefficients for different rates for U_1, U_2 and the overall system. It has been observed that when the rate increases, so does the SOP. It also demonstrates how modifying the power distribution coefficients will result in the lowest SOP for different threshold rates for U_1, U_2 and the whole system. For each rate, U_1 has a coefficient with the lowest SOP. Following the low point, the curve progressively approaches the ceiling, suggesting that the ceiling impact has been activated. For U_2, meanwhile, it is seen that the SOP continues to decrease for all coefficients once they are big enough to overcome the ceiling effect. The entire system plot also displays the lowest point for the specified rates, indicating the optimal allocation coefficients for the entire system.

Figure-5.5 compares NOMA's secrecy performance with an OMA strategy that uses time splitting to accommodate two users. With a power allocation coefficient of $a_1 = 0.05$, it appears that OMA has a smaller SOP than NOMA in the event of a nearby user. This is due to the reason that NOMA does not provide adequate power to the near-user section of the signal. However, NOMA outperforms OMA for long-distance users. Overall, OMA outperforms NOMA in the higher SNR regime.

Figure-5.6 demonstrates that NOMA and OMA can operate similarly for the proper power distribution coefficient, for the close user, excepting at the rate R= 4, due to the ceiling effect for NOMA. The distant user continues to outperform OMA in NOMA. At greater SNR levels, the entire system performance converges.

In Figure-5.7, wherein $a_1 = 0.2$, U_1 demonstrates superior SOP performance than OMA when NOMA is used, since the NOMA scheme obtains a larger power coefficient. Similar to prior situations, for U_2, NOMA outperforms OMA. For the entire system, NOMA performs superior to OMA for all SNR values evaluated, with the exception of rates where the ceiling effect is apparent.

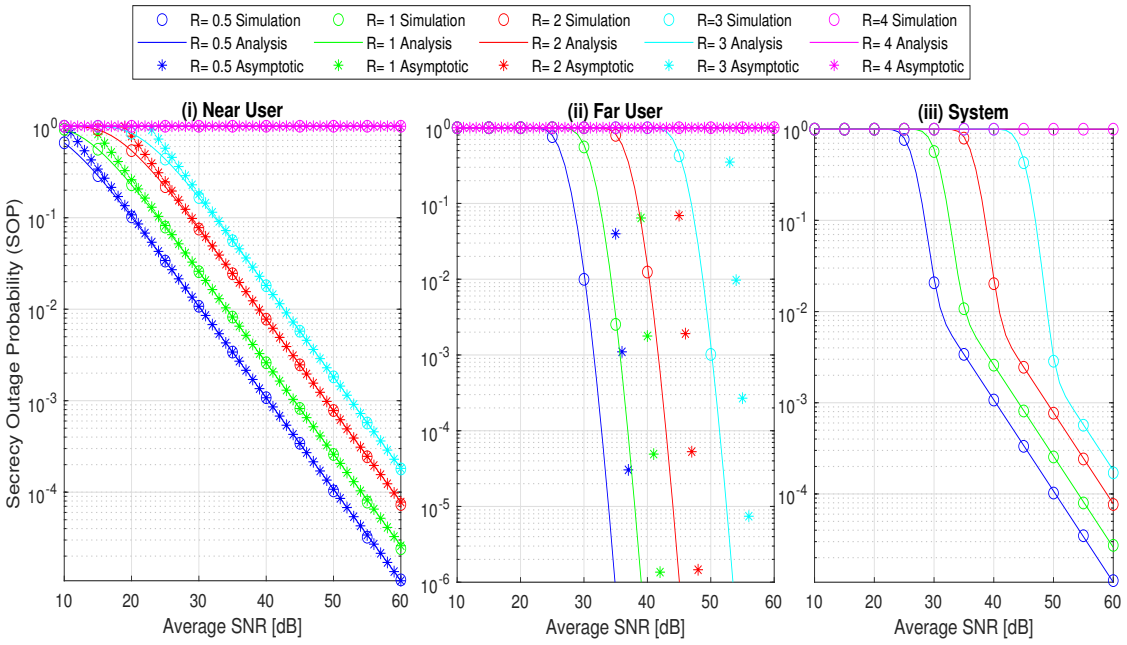

Figure 5.1: SOP vs SNR with change in rate for n = 15 , $a_1 = 0.1$

Figure 5.8 demonstrates that the verification loss is smaller than the training loss, suggesting that the model's prediction ability is good. Also, the validation loss curve which follows the training loss curve indicates that the training went successfully. Figure 5.9 shows that the model's prediction capacity improves as the dots go closer to the line. The RMSE figures are 6.895×10^{-4} and 9.11×10^{-4} for close and far users, respectively.

Figures 5.10 and 5.11 depict the DNN's prediction for power coefficient values $a_1 = 0.05$ and $a_1 = 0.1$, respectively. The graphs show that the forecast is approximately as accurate as 10^{-3}. The key difference between the DNN assessment, mathematical evaluation, and Monte Carlo simulation regarding the proposed system is the execution time. The results show that generating SOP values using DNN prediction takes just 82.6 milliseconds, but mathematical evaluation takes 111.7 milliseconds and a Monte Carlo simulation takes 6.032 seconds.

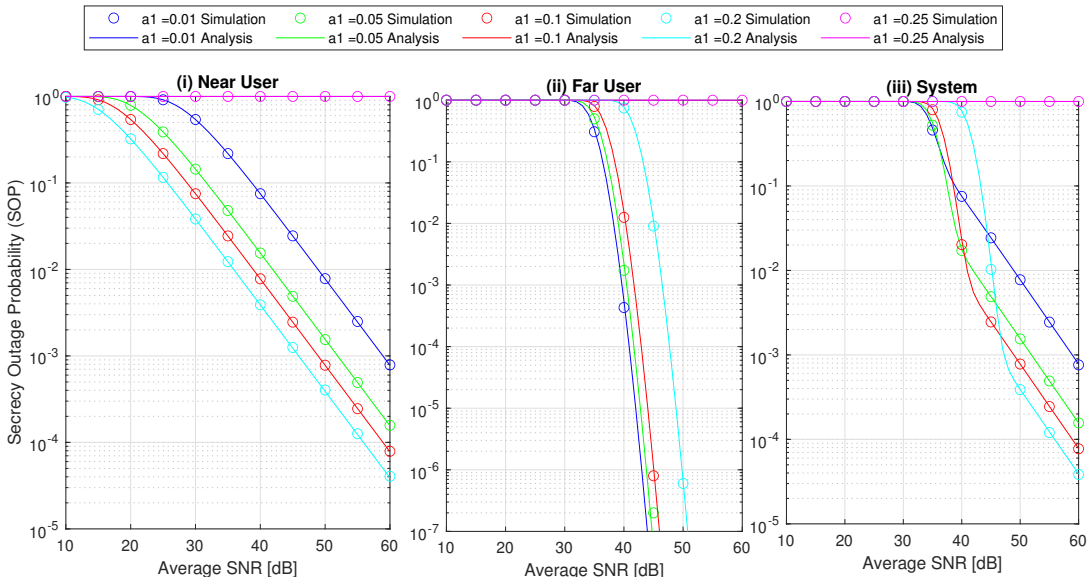

Figure 5.2: SOP vs SNR with change in allocation coefficient for far user for n = 15 , R = 2 bps/ Hz

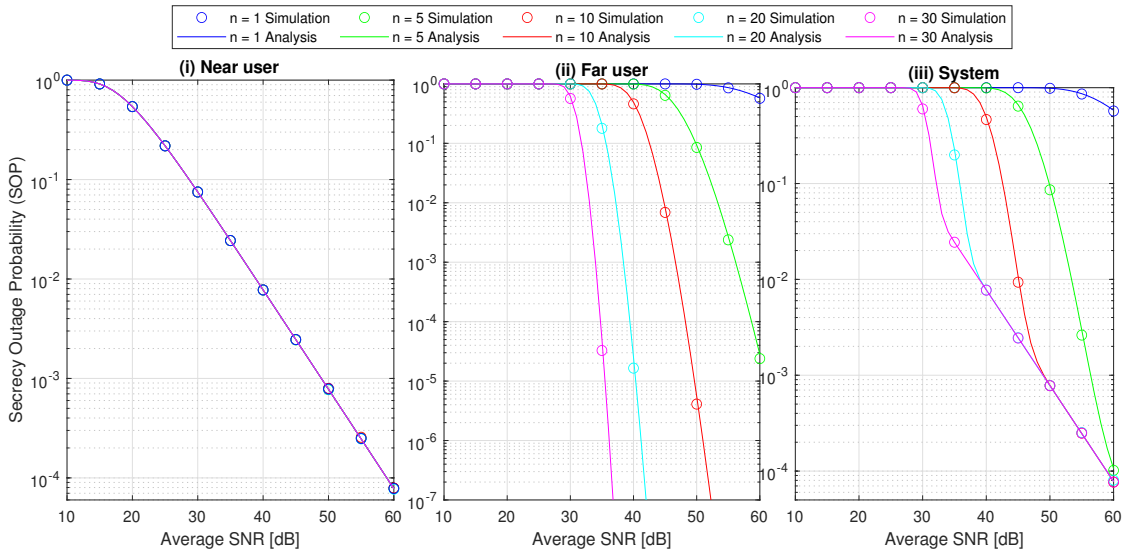

Figure 5.3: SOP vs SNR with change in no. of RIS elements for far user for R= 2 bps/ Hz, $a_1 = 0.1$

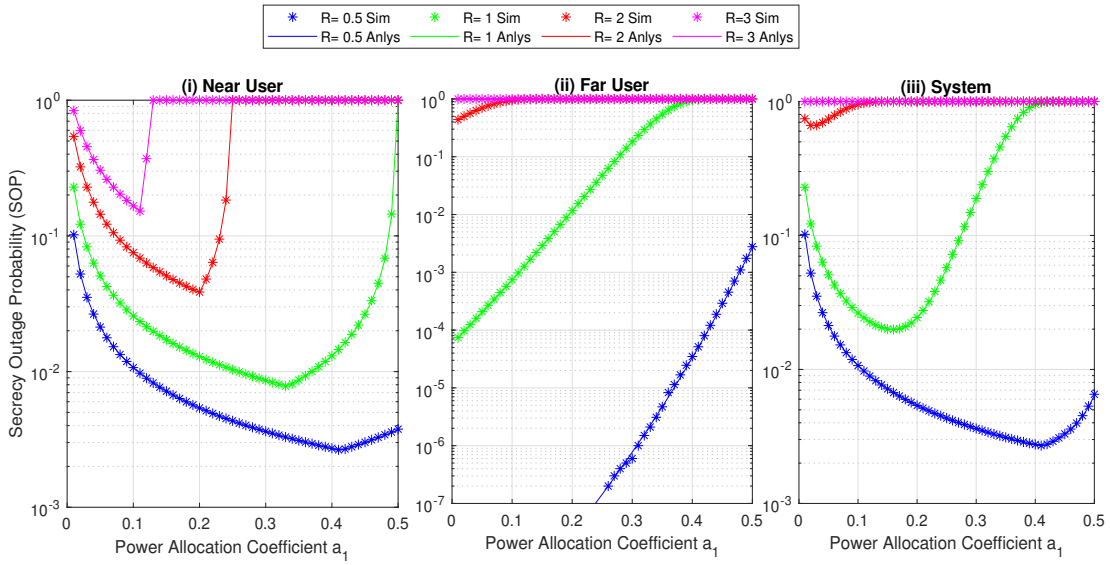

Figure 5.4: SOP vs Power allocation coefficients with change in rates for n = 25 and average SNR = 30 dB

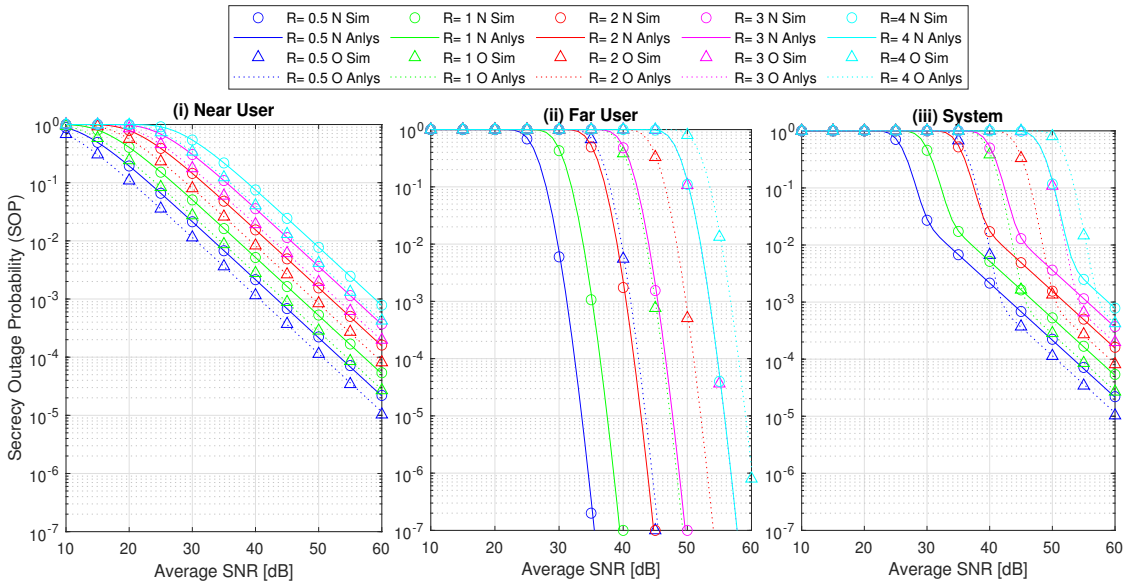

Figure 5.5: SOP vs SNR with change in rates comparing NOMA and OMA schemes for n = 15 and $a_1 = 0.05$

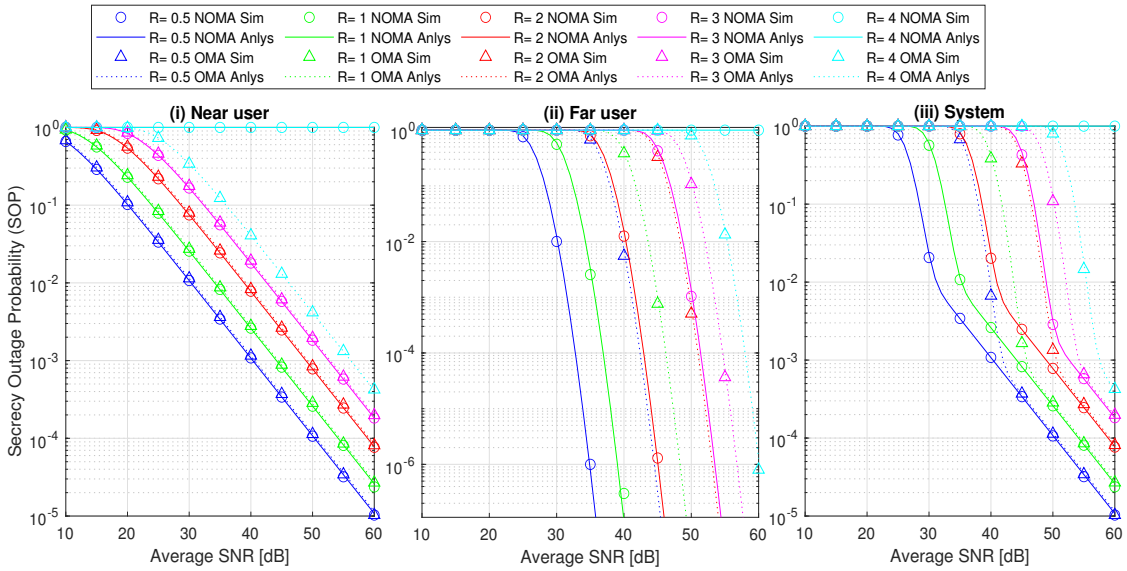

Figure 5.6: SOP vs SNR with change in rates comparing NOMA and OMA schemes for n = 15 and $a_1 = 0.1$

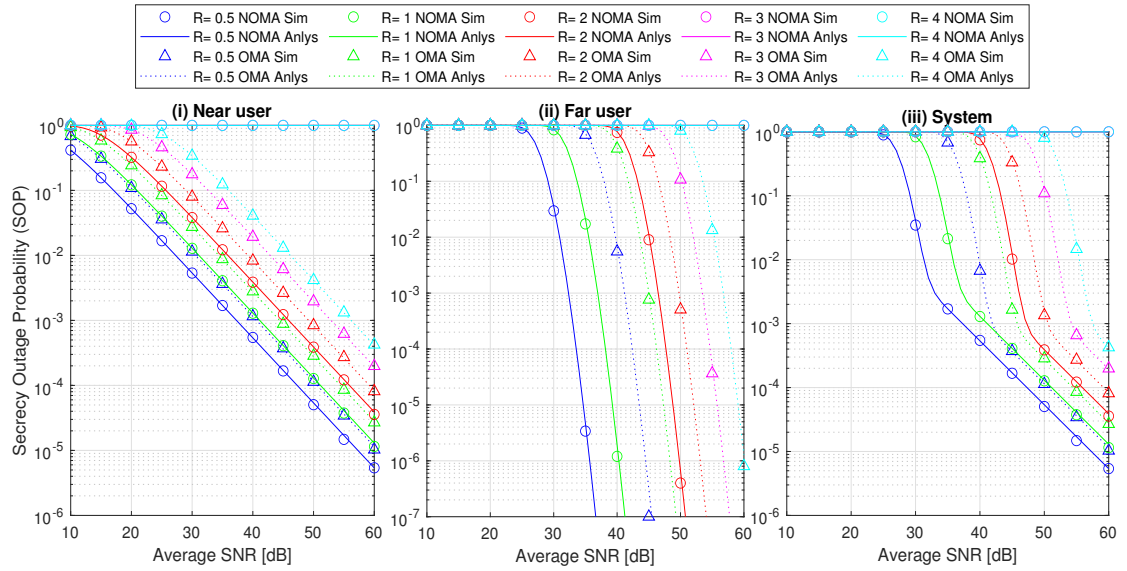

Figure 5.7: SOP vs SNR with change in rates comparing NOMA and OMA schemes for n = 15 and $a_1 = 0.2$

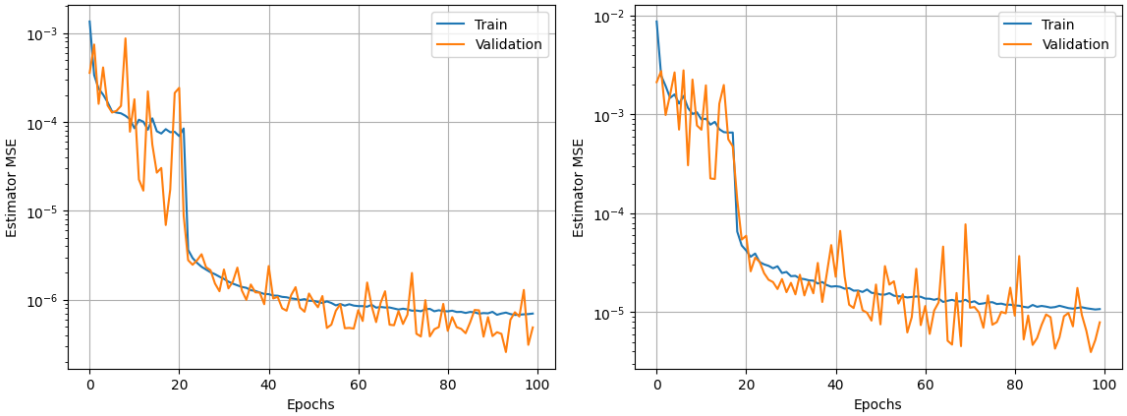

(a) Near user (b) Far user

Figure 5.8: Training and validation losses vs Epochs

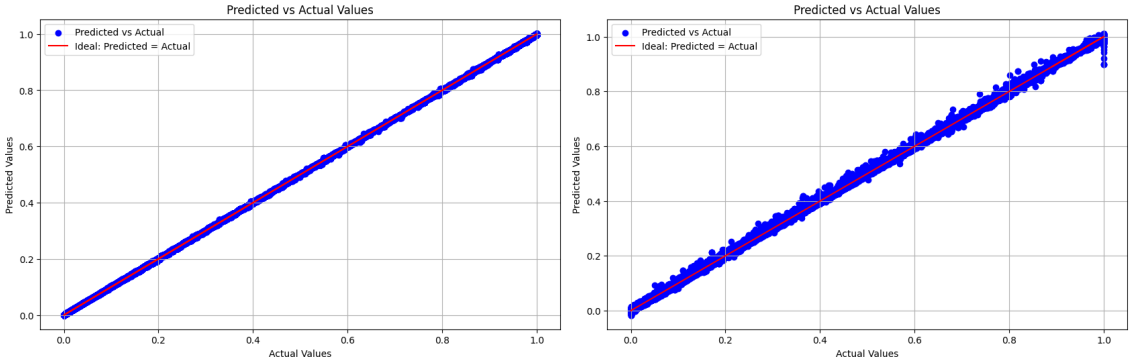

(a) Near user (b) Far user

Figure 5.9: Comparing predictions with true values

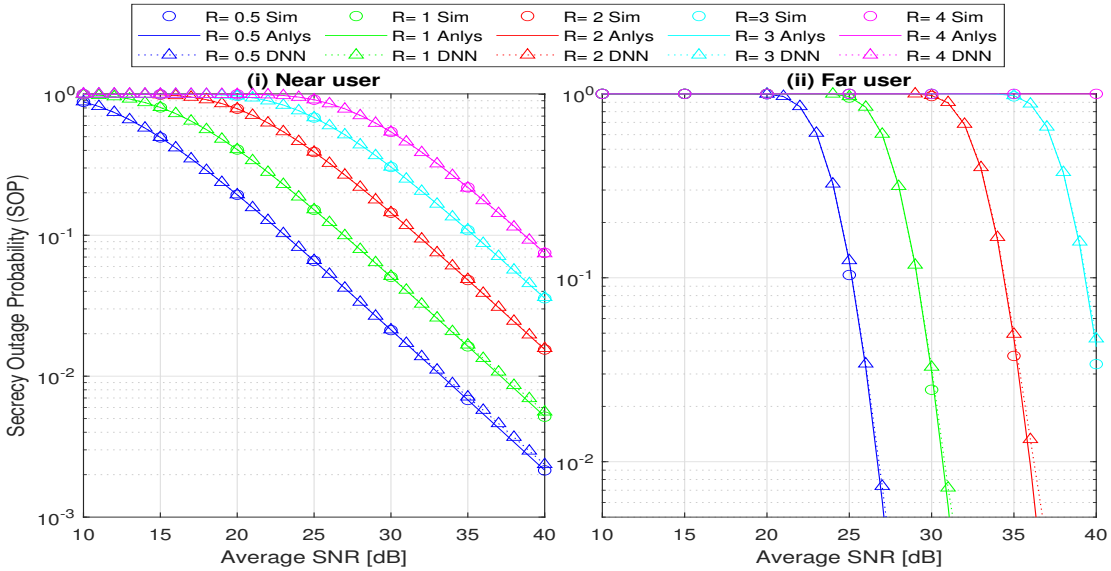

Figure 5.10: DNN Prediction vs analysis comparison for n= 20, $a_1 = 0.05$

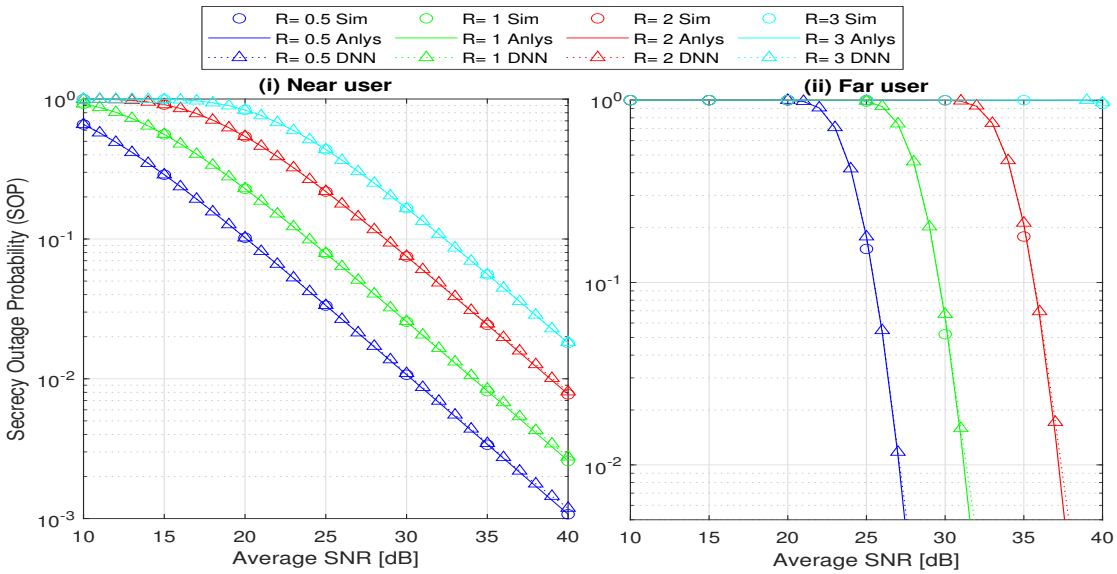

Figure 5.11: DNN Prediction vs analysis comparison for n= 20, $a_1 = 0.1$

CHAPTER 6

CONCLUSIONS AND FUTURE WORKS

In this chapter, the conclusions derived from the work in this thesis are presented and the possible directions for the future works are provided.

6.1 Conclusions

The secrecy performance of a UAV-borne RIS NOMA system outfitted with a jammer and a malicious eavesdropper was evaluated. To evaluate the system's effectiveness, new channel gain formulations for UAV-to-ground channels were created by investigating the appropriate channel features of the LoS Rician fading connections. Closed-form expressions for NOMA users' SOPs were developed to assess performance. To gather additional data, asymptotic estimates in the very high SNR zone were employed to compute the diversity order for the two users. The diversity order was found to be determined by both the amount of RIS reflecting components and the Rician fading factors. In this scenario, altering the number of RIS components proved to be beneficial up to a point. The whole system performance was evaluated to establish the optimal power allocation values for various rates. The SOP's dependency upon the jammer signal was additionally evaluated. NOMA was shown to surpass its orthogonal counterpart in terms of power allocation coefficient. Finally, a DNN model that can anticipate secrecy efficiency while accounting for a changing environment was developed. It demonstrated the capacity to accurately anticipate the SOP to a maximum of two places in decimal.

6.2 Future Works

With emerging 5G communication, there are many open problems related to the topics of this thesis that could be treated in future research. Some future prospects for the research work are given in the sequel.

This project explored a two-user UAV-aided RIS NOMA system, but this can be extended to include more than two users in a user group that share the same spectral resources. In such a scenario, it will be interesting to explore the methods of configuring the RIS to optimize the channel gains of all the legitimate users. Also, the secrecy performance of this system might lead to some unique insights.

The inclusion of simultaneous transmitting and receiving RIS (STAR-RIS) is another exciting path that can be researched. With the serving range of RIS extended, it can manipulate its environment even more effectively. Secrecy capacity is expected to improve but the finer details are yet to be explored.

With the above mentioned prospects, the existing body of knowledge in the design of can be further expanded.

REFERENCES

[1] "IMT Traffic estimates for the years 2020 to 2030," ITU, Jul. 2015. https://www.itu.int/en/publications/ITU-R/Pages/publications.aspx?parent=R-REP-M.2370.

[2] L. Vailshery, "IoT Connected Devices Worldwide 2019-2030," Statista, Jul. 27, 2023. https://www.statista.com/statistics/1183457/iot-connected-devices-worldwide/

[3] X. Yuan, Y. -J. A. Zhang, Y. Shi, W. Yan and H. Liu, "Reconfigurable-Intelligent-Surface Empowered Wireless Communications: Challenges and Opportunities," in IEEE Wireless Communications, vol. 28, no. 2, pp. 136-143, April 2021.

[4] M. Mozaffari, W. Saad, M. Bennis, Y. -H. Nam and M. Debbah, "A Tutorial on UAVs for Wireless Networks: Applications, Challenges, and Open Problems," in IEEE Communications Surveys & Tutorials, vol. 21, no. 3, pp. 2334-2360, third quarter 2019.

[5] Z. Ding, X. Lei, G. K. Karagiannidis, R. Schober, J. Yuan and V. K. Bhargava, "A Survey on Non-Orthogonal Multiple Access for 5G Networks: Research Challenges and Future Trends," in IEEE Journal on Selected Areas in Communications, vol. 35, no. 10, pp. 2181-2195, Oct. 2017.

[6] Y. Zou, J. Zhu, X. Wang and L. Hanzo, "A Survey on Wireless Security:

Technical Challenges, Recent Advances, and Future Trends," in Proceedings of the IEEE, vol. 104, no. 9, pp. 1727-1765, Sept. 2016.

[7] L. Yang, F. Meng, J. Zhang, M. O. Hasna and M. D. Renzo, "On the Performance of RIS-Assisted Dual-Hop UAV Communication Systems," in IEEE Transactions on Vehicular Technology, vol. 69, no. 9, pp. 10385-10390, Sept. 2020.

[8] T. Shafique, H. Tabassum and E. Hossain, "Optimization of Wireless Relaying With Flexible UAV-Borne Reflecting Surfaces," in IEEE Transactions on Communications, vol. 69, no. 1, pp. 309-325, Jan. 2021.

[9] Y. Cai, Z. Wei, S. Hu, C. Liu, D. W. K. Ng and J. Yuan, "Resource Allocation and 3D Trajectory Design for Power-Efficient IRS-Assisted UAV-NOMA Communications," in IEEE Transactions on Wireless Communications, vol. 21, no. 12, pp. 10315-10334, Dec. 2022.

[10] C. K. Singh, P. K. Upadhyay, J. Lehtomäki and M. Juntti, "Outage Performance with Deep Learning Analysis for UAV-Borne IRS Relaying NOMA Systems with Hardware Impairments," 2022 IEEE 96th Veh. Tech. Conf.(VTC2022-Fall), London, United Kingdom, 2022, pp. 1-7.

[11] L. Bariah, F. Boukhalfa, W. Jaafar, S. Muhaidat and H. Yanikomeroglu, "On the Performance of RIS-enabled NOMA for Aerial Networks," 2023 IEEE Wireless Communications and Networking Conference (WCNC), Glasgow, United Kingdom, 2023, pp. 1-6.

[12] Z. Tang, T. Hou, Y. Liu, J. Zhang, and L. Hanzo, "Physical Layer Security of Intelligent Reflective Surface Aided NOMA Networks," IEEE Transactions on Vehicular Technology, vol. 71, no. 7, pp. 7821–7834, Jul. 2022.

[13] W. Wang, H. Tian and W. Ni, "Secrecy Performance Analysis of IRS-Aided UAV Relay System," in IEEE Wireless Communications Letters, vol. 10, no. 12, pp. 2693-2697, Dec. 2021.

[14] T. T. Nguyen, V. T. Hoang, T. T. Huyen Le and X. N. Tran, "Physical Layer Security for UAV-Based Full-Duplex Relay NOMA System," 2022 International Conference on Advanced Technologies for Communications (ATC), Ha Noi, Vietnam, 2022, pp. 395-400.

[15] H. Yang, S. Liu, L. Xiao, Y. Zhang, Z. Xiong and W. Zhuang, "Learning-Based Reliable and Secure Transmission for UAV-RIS-Assisted Communication Systems," in IEEE Transactions on Wireless Communications, DOI 10.1109/TWC.2023.3336535.

[16] Y. Cheng, J. Lu, D. Niyato, B. Lyu, M. Xu and S. Zhu, "Performance Analysis of Jammer-Aided Covert RIS-NOMA Systems," GLOBECOM 2022 - 2022 IEEE Global Communications Conference, Rio de Janeiro, Brazil, 2022, pp. 2716-2721.

[17] Y. Zhou, P. L. Yeoh, H. Chen, Y. Li, W. Hardjawana and B. Vucetic, "Secrecy Outage Probability and Jamming Coverage of UAV-enabled Friendly Jammer," 2017 11th International Conference on Signal Processing and Communication Systems (ICSPCS), Surfers Paradise, Australia, 2017, pp. 1-6.

[18] V. N. Vo, C. So-In, H. Tran, D. -D. Tran and T. P. Huu, "Performance Analysis of an Energy-Harvesting IoT System Using a UAV Friendly Jammer and NOMA Under Cooperative Attack," in IEEE Access, vol. 8, pp. 221986-222000, 2020.

[19] D. Diao, B. Wang, K. Cao, R. Dong and T. Cheng, "Enhancing Reliability and Security of UAV-Enabled NOMA Communications With Power Allocation and Aerial Jamming," in IEEE Transactions on Vehicular Technology, vol. 71, no. 8, pp. 8662-8674, Aug. 2022.

[20] K. Yadav, P. K. Upadhyay and M. Magarini, "Physical Layer Security Analysis of IRS-Aided UAV Relaying Systems with NOMA," 2023 IEEE International Mediterranean Conference on Communications and Networking (MeditCom), Dubrovnik, Croatia, 2023, pp. 157-163,

[21] D. Wang, Y. Zhao, Y. Lou, L. Pang, Y. He and D. Zhang, "Secure NOMA Based RIS-UAV Networks: Passive Beamforming and Location Optimization," GLOBECOM 2022 - 2022 IEEE Global Communications Conference, Rio de Janeiro, Brazil, 2022, pp. 3168-3173.

[22] H. Huang et al., "Deep learning for physical-layer 5G wireless techniques: Opportunities, challenges and solutions," IEEE Wireless Commun., vol. 27, no. 1, pp. 214-222, Feb. 2020.

[23] T. Jiang, H. V. Cheng, and W. Yu, "Learning to reflect and to beamform for intelligent reflecting surface with implicit channel estimation," IEEE J. Sel. Areas Commun., vol. 39, no. 7, pp. 1931–1945, Jul. 2021.

[24] H. Song, M. Zhang, J. Gao, and C. Zhong, "Unsupervised learning based joint active and passive beamforming design for reconfigurable intelligent surfaces aided wireless networks," IEEE Commun. Lett., vol. 25, no. 3, pp. 892–896, Mar. 2021.

[25] A. Al-Hourani and K. Gomez, "Modeling Cellular-to-UAV Path-Loss for Suburban Environments," IEEE Wireless Communications Letters, vol. 7, no. 1, pp. 82–85, Feb. 2018.

[26] A. M. Salhab and M. H. Samuh, "Accurate Performance Analysis of Reconfigurable Intelligent Surfaces Over Rician Fading Channels," IEEE Wireless Communications Letters, vol. 10, no. 5, pp. 1051–1055, May 2021.

[27] I. S. Gradshteyn and I. M. Ryzhik, Tables of Integrals, Series and Products, 7th ed. New York: Academic Press, 2007.